Monthly Notices
of the
ROYAL ASTRONOMICAL SOCIETY

MNRAS **489,** 3939–3952 (2019)
Advance Access publication 2019 September 13

doi:10.1093/mnras/stz2410

Constraints on high-J CO emission lines in $z \sim 6$ quasars

S. Carniani,[1★] S. Gallerani,[1] L. Vallini,[2,3] A. Pallottini,[1,4] M. Tazzari,[5] A. Ferrara,[1] R. Maiolino,[6,7] C. Cicone,[8] C. Feruglio,[9] R. Neri,[10] V. D'Odorico,[1,9] R. Wang[11] and J. Li[12]

[1]*Scuola Normale Superiore, Piazza dei Cavalieri 7, I-56126 Pisa, Italy*
[2]*Leiden Observatory, PO Box 9513, NL-2300 RA Leiden, the Netherlands*
[3]*Nordita, KTH Royal Institute of Technology and Stockholm University, Roslagstullsbacken 23, SE-10691 Stockholm, Sweden*
[4]*Centro Fermi, Museo Storico della Fisica e Centro Studi e Ricerche 'Enrico Fermi', Piazza del Viminale 1, I-00184 Roma, Italy*
[5]*Institute of Astronomy, University of Cambridge, Madingley Road, Cambridge CB3 0HA, UK*
[6]*Kavli Institute for Cosmology, University of Cambridge, Madingley Road, Cambridge CB3 0HA, UK*
[7]*Cavendish Laboratory, University of Cambridge, 19 J. J. Thomson Ave., Cambridge CB3 0HE, UK*
[8]*INAF – Osservatorio Astronomico di Brera, Via Brera 28, I-20121 Milano, Italy*
[9]*INAF – Osservatorio Astronomico di Trieste, Via G. Tiepolo 11, I-34143, Trieste, Italy*
[10]*Institute de Radioastronomie Millimetrique, F-38406 St Martin d'Heres, France*
[11]*Kavli Institute of Astronomy and Astrophysics at Peking University, No. 5 Yiheyuan Road, Haidian District, Beijing 100871, China*
[12]*Department of Astronomy, School of Physics, Peking University, Beijing 100871, China*

Accepted 2019 August 21. Received 2019 July 29; in original form 2019 February 4

ABSTRACT

We present Atacama Large Millimeter/submillimeter Array (ALMA) observations of eight highly excited CO ($J_{up} > 8$) lines and continuum emission in two $z \sim 6$ quasars: SDSS J231038.88+185519.7 (hereafter J2310), for which CO(8–7), CO(9–8), and CO(17–16) lines have been observed, and ULAS J131911.29+095951.4 (J1319), observed in the CO(14–13), CO(17–16), and CO(19–18) lines. The continuum emission of both quasars arises from a compact region (<0.9 kpc). By assuming a modified blackbody law, we estimate dust masses of $\log(M_{dust}/M_\odot) = 8.75 \pm 0.07$ and $\log(M_{dust}/M_\odot) = 8.8 \pm 0.2$ and dust temperatures of $T_{dust} = 76 \pm 3$ K and $T_{dust} = 66^{+15}_{-10}$ K, respectively, for J2310 and J1319. Only CO(8–7) and CO(9–8) in J2310 are detected, while 3σ upper limits on luminosities are reported for the other lines of both quasars. The CO line luminosities and upper limits measured in J2310 and J1319 are consistent with those observed in local active galactic nuclei and starburst galaxies, and other $z \sim 6$ quasars, except for SDSS J1148+5251 (J1148), the only quasar at $z = 6.4$ with a previous CO(17–16) line detection. By computing the CO spectral line energy distributions normalized to the CO(6–5) line and far-infrared luminosities for J2310, J1319, and J1148, we conclude that different gas heating mechanisms (X-ray radiation and/or shocks) may explain the different CO luminosities observed in these $z \sim 6$ quasar. Future $J_{up} > 8$ CO observations will be crucial to understand the processes responsible for molecular gas excitation in luminous high-z quasars.

Key words: galaxies: active – galaxies: high-redshift – galaxies: ISM – quasars: individual: SDSS J231038.88+185519.7 – quasars: individual: ULAS J131911.29+095951.4.

1 INTRODUCTION

The presence of early supermassive black holes (SMBHs) represents a challenging problem in modern cosmology. In the last decades, more than 200 quasars have been discovered at $z \sim 6$ and beyond (e.g. Bañados et al. 2016, 2018; Jiang et al. 2016; Matsuoka et al. 2016, 2018; Mazzucchelli et al. 2017); for several of them, the mass of the hosted black holes (BHs) has been measured and found to be $M_{BH} \sim (0.02–1.1) \times 10^{10}\,M_\odot$ (Jiang et al. 2007; Kurk et al. 2007; Willott et al. 2010; De Rosa et al. 2011; Wu et al. 2015; Feruglio et al. 2018). The presence of such SMBHs when the Universe was less than 1 Gyr old is still an open problem (Li et al. 2007; Narayanan et al. 2008; Volonteri 2010; Di Matteo et al. 2012; Valiante et al. 2017), deeply connected both with the galaxy–BH coevolution (e.g. Lamastra et al. 2010; Wang et al. 2010; Volonteri & Stark 2011;

★ E-mail: stefano.carniani@sns.it

Valiante et al. 2014) and the contribution of quasars to the cosmic reionization process (Volonteri & Gnedin 2009; Giallongo et al. 2015; Madau & Haardt 2015; Manti et al. 2017; Qin et al. 2017; Mitra, Choudhury & Ferrara 2018; Parsa, Dunlop & McLure 2018; Kulkarni, Worseck & Hennawi 2019).

In the last years, the advent of millimetre and submillimetre interferometers has given the possibility of studying the physical properties of the interstellar medium (ISM) in $z \sim 6$ galaxies hosting SMBHs. In fact, several important tracers of the ISM physical and chemical state, such as the [C II] line at 158 μm, CO rotational transitions, and dust continuum emission, are redshifted in the millimetre bands at high redshift and are observable from ground-based facilities (see Gallerani et al. 2017a, for a review on this topic). The Atacama Large Millimeter/submillimeter Array (ALMA) is currently the most powerful interferometer for observing rest-frame far-infrared (FIR) emission in the distant Universe, as highlighted in several recent works showing ALMA capabilities on investigating ISM properties in $z > 4$ quasars (Gallerani et al. 2012; Carniani et al. 2013; Decarli et al. 2017, 2018; Venemans et al. 2017a,b; Bischetti et al. 2018; Feruglio et al. 2018).

In this work we focus on CO, the most abundant molecule after H_2 (Carilli & Walter 2013). CO has a finite dipole moment that allows transitions between energy levels with small energy gaps. Examining the CO spectral line energy distribution (SLED), which is the relative luminosity (or intensity) of CO lines as a function of rotational transitions J_{up}, provides us the opportunity to probe the excitation conditions of molecular gas in galaxies. This kind of observations will not be possible with the fainter quadrupole transitions of H_2 until the advent of SPace IR telescope for Cosmology and Astrophysics (SPICA; Spinoglio et al. 2017; Egami et al. 2018).

The strength of low-J and mid-J transitions ($J_{up} < 6$) is mainly driven by physical properties such as gas density and temperature (e.g. Obreschkow et al. 2009; Mashian et al. 2015). At high redshift ($z \sim 6$) the shape of the CO SLED also depends on the cosmic microwave background (CMB) radiation (da Cunha et al. 2013), since the CMB temperature ($T_{CMB} \sim 20$ K) becomes comparable to that of the cold/molecular gas (∼10–50 K). The high T_{CMB} increases the gas excitation conditions and boosts the CO line intensities. At the same time, the CMB background against which the line is measured increases too. This twofold effect shifts the peak of the CO SLED at higher transitions up to $J_{up} \sim 6$–7 (Tunnard & Greve 2016; Vallini et al. 2018). Mid-J CO observations can be therefore used in the early Universe for investigating the molecular gas reservoir and ISM properties in both star-forming (e.g. Genzel et al. 2015; Aravena et al. 2016) and quasar host galaxies (e.g. Carniani et al. 2017b; Kakkad et al. 2017; Venemans et al. 2017a,b; Brusa et al. 2018).

High-J ($J_{up} \geq 7$) CO lines are only emitted from states with temperatures 150–7000 K above the ground and have critical densities of 10^5–10^8 cm^{-3}. These lines trace molecular warm and dense gas and are often overluminous in extreme environments, such as luminous active galactic nucleus (AGN; e.g. Meijerink, Spaans & Israel 2007; Schleicher, Spaans & Klessen 2010), extreme starbursts [star formation rate (SFR) > 1000 $M_\odot$ yr^{-1}; e.g. Narayanan et al. 2008], and regions shocked by merging or outflows mechanisms (Panuzzo et al. 2010; Hailey-Dunsheath et al. 2012; Richings & Faucher-Giguère 2018). Identifying the dominant mechanism for molecular gas excitation is crucial for a proper interpretation of high-J CO line observations, and thus for a deeper understanding of the ISM properties.

In the local Universe high-J CO lines have been detected by using the Photodetector Array Camera and Spectrometer (PACS; Poglitsch et al. 2010) onboard of the *Herschel Space Observatory* (Pilbratt et al. 2010). Mashian et al. (2015) reported the high-J CO SLED ($14 \leq J_{up} \leq 50$) of five starburst galaxies, five AGN, 22 ULIRGs, and two interacting systems. They found that the extreme diversity in CO emission makes multiple lines essential to constrain the gas properties.

At high-z, $J_{up} > 7$ CO transitions have been observed only in quasars and extreme starburst galaxies (Weiß et al. 2007; Riechers et al. 2013; Gallerani et al. 2014; Venemans et al. 2017b). In particular, Gallerani et al. (2014) detected with the Plateau de Bure interferometer (PdBI) an exceptionally strong CO(17–16) line in the $z = 6.4$ quasar SDSS J114816.64+525150.3 (hereafter J1148). By combining previous CO observations (Bertoldi et al. 2003b; Walter et al. 2003; Riechers et al. 2009) with the detection of the CO(17–16), and by comparing the observed CO SLED with photodissociation region (PDR) and X-ray-dominated region (XDR) models (Meijerink & Spaans 2005; Meijerink et al. 2007), the authors found that while PDR models can fairly reproduce the observed CO SLED for $J_{up} < 7$, the CO(17–16) line can only be explained through the presence of a substantial X-ray radiation field. Indeed, strong X-ray emission ($L_X \sim 10^{45}$ erg s^{-1}) was recently detected in this source (Gallerani et al. 2017b), supporting the idea that high-J CO transitions may be used to infer the presence of X-ray faint or obscured SMBH progenitors in galaxies at $z > 6$. Since J1148 is the unique source where high-J CO lines have been detected so far at high redshift, these results motivated further observations of highly excited CO lines in $z \sim 6$ quasars.

In this work, we present ALMA observations of six high-J CO lines and continuum emission in the $z \sim 6$ quasars SDSS J231038.88+185519.7 (hereafter J2310) at $z = 6.00$ and ULAS J131911.29+095951.4 (hereafter J1319) at $z = 6.13$. We reanalyse the FIR emission and CO SLED of SDSS J1148+5251, and compare the properties of these three quasars. This paper is organized as follows. The two targets are presented in Section 2, while ALMA observations are described in Section 3. In Section 4, we present continuum and CO emission properties of the three quasars. In Section 5, we compare our results with local and high-z observations. We discuss and summarize our findings in Sections 6 and 7, respectively. We adopt the cosmological parameters from Planck Collaboration XIII (2016): $H_0 = 67.7$ km s^{-1} Mpc^{-1}, $\Omega_m = 0.308$, and $\Omega_\Lambda = 0.70$, according to which 1 arcsec at $z = 6$ corresponds to a proper distance of 5.84 kpc.

2 TARGETS

2.1 J2310

With a magnitude $m_{1450} = 19.30$, J2310 is one of the brightest $z \sim 6$ quasar in the Sloan Digital Sky Survey. By using the ultraviolet (UV) lines of C IV and Mg II, Jiang et al. (2016) and Feruglio et al. (2018) estimate a BH mass $M_{BH} = (1.8 \pm 0.5) \times 10^9$ $M_\odot$ that is 2.5 per cent of the dynamical mass recently inferred from high angular ALMA observations of CO(6–5) line (Feruglio et al. 2018). The estimated dynamical and BH masses place J2310 above the local M_{dyn}–M_{BH} relation, similarly to most of the quasars studied at these redshifts (Wang et al. 2013; Decarli et al. 2018).

Over the last years J2310 has been also studied extensively in the millimetre bands. FIR line observations of [C II] at 158 μm and [O III] at 88 μm have been reported by Wang et al. (2013) and Hashimoto et al. (2018), respectively.

Table 1. Description of the continuum observations and derived characteristics.

Source	z	$\nu_{\rm cont}$	$\sigma_{\rm cont}$	$S_{\rm cont}$	Angular	Half-light	Ell.	PA	Reference
		(GHz)	(μJy beam^{-1})	(mJy)	resolution (arcsec)	radius (arcsec)		(°)	
(a)	(b)	(c)	(d)	(e)	(f)	(g)	(h)	(i)	(j)
J2310	6.0031	91.5	5	0.416 ± 0.033	0.5 × 0.3	0.12 ± 0.02	0.5 ± 0.3	138 ± 24	[1]
		99	50	0.40 ± 0.05	5.4 × 3.9	–	–	–	[3]
		132	15	1.39 ± 0.03	0.75 × 0.71	0.10 ± 0.02	<0.9	100 ± 60	This work
		141	15	1.42 ± 0.02	0.81 × 0.66	0.09 ± 0.02	<0.2	100 ± 60	This work
		250	630	8.29 ± 0.63	11	–	–	–	[3]
		263	80	8.91 ± 0.08	0.7	0.12 ± 0.02	0.2 ± 0.1	162 ± 18	[2]
		280	42	12.0 ± 0.2	0.51 × 0.39	0.105 ± 0.016	<0.12	160 ± 40	This work
		484	362	24.9 ± 0.7	0.69 × 0.60	0.15 ± 0.02	0.3 ± 0.2	154 ± 32	[4]
J1319	6.1330	97	80	0.31 ± 0.08	∼3.5	–	–	–	[2]
		233	45	3.89 ± 0.12	1.59 × 1.03	0.13 ± 0.02	<0.2	110 ± 70	This work
		250	650	4.20 ± 0.65	∼11	–	–	–	[2]
		258	100	5.23 ± 0.10	∼0.7	0.19 ± 0.01	0.12 ± 0.08	121 ± 148	[3]
		267	43	6.03 ± 0.07	1.40 × 0.97	0.13 ± 0.02	<0.2	70 ± 70	This work
		306	42	7.39 ± 0.11	0.51 × 0.38	0.139 ± 0.005	0.12 ± 0.07	55 ± 11	This work
		347	33	9.68 ± 0.12	0.78 × 0.51	0.143 ± 0.008	0.17 ± 0.05	55 ± 20	This work

Note. Column (a): object name. Column (b): redshift. Column (c): observed frequency. Column (d): rms on the continuum. Column (e): continuum flux density. Column (f): angular resolution. Column (g): half-light radius $R_{\rm e}$ of continuum emission. We note that in literature the galaxy size is usually reported in term of either full width at half-maximum (FWHM), if a Gaussian profile has been used as model, or radius scale $r_{\rm d}$, in the case of an exponential profile model. $R_{\rm e}$ is related to FWHM and $r_{\rm d}$ as $R_{\rm e} \approx \sqrt{-2\ln(0.5)}{\rm FWHM}/2.355$ and $R_{\rm e} \approx 1.67835 r_{\rm d}$, respectively. Column (h): ellipticity. Column (i): position angle. Column (j): reference: [1] Feruglio et al. (2018); [2] Wang et al. (2013); [3] Wang et al. (2011); and [4] Hashimoto et al. (2018).

2.2 J1319

J1319 was initially discovered in the UKIRT Infrared Deep Sky Survey (UKIDSS) by Mortlock et al. (2009), who measured an optical magnitude of $m_{1450} = 19.65$ and identified its redshift from the Lyα and Mg II emission lines. Shao et al. (2017) estimate a BH mass $M_{\rm BH} = (2.7 \pm 0.6) \times 10^9$ M$_\odot$ from the Mg II line, which contributes 2 per cent of the dynamical mass of the system. The BH-to-dynamical mass ratio is four times larger than the average $M_{\rm BH}/M_{\rm dyn}$ measured locally (Kormendy & Ho 2013).

Several millimetre observations have been carried out of this quasar covering the frequency range between 1.4 and 300 GHz, revealing a high FIR emission ($>10^{13}$ L$_\odot$) from the host galaxy (Wang et al. 2011, 2013). The quasar has been also detected in both CO(6–5) and [C II] at 158 μm (Wang et al. 2011, 2013).

3 OBSERVATIONS

In ALMA Cycle 2 project 2013.1.00462.S (PI: S. Gallerani) we proposed high-J CO observations of the $z \sim 6$ quasars J2310 and J1319 that have been already observed in CO(6–5) (Wang et al. 2013; Feruglio et al. 2018). We requested ALMA time to observe the molecular line CO(17–16) at $\nu_{\rm rest} = 1956.02$ GHz ($\nu_{\rm obs} = 279.31$ GHz) for J2310, and three high-J CO transitions, CO(14–13) at $\nu_{\rm rest} = 1611.79$ GHz ($\nu_{\rm obs} = 225.96$ GHz), CO(17–16) ($\nu_{\rm obs} = 274.22$ GHz), and CO(19–18) at $\nu_{\rm rest} = 2185.13$ GHz ($\nu_{\rm obs} = 306.34$ GHz), for J1319. ALMA band 6 and 7 observations were obtained between 2015 January and June, using 34–40 antennas with baselines from 15 to 700 m. In each observations, one out of the four 1.8 GHz spectral windows was centred at the CO frequency and the other three were used to sample the rest-frame FIR continuum emission. The spectral channel width was set up in time domain mode with a spectral resolution of 31.250 MHz, corresponding to ∼20 km s^{-1} velocity resolution at the line frequencies. For each CO observations we spent between 13 and 31 min on source, reaching a continuum sensitivity of ∼42 μJy beam^{-1} and a spectral sensitivity of 0.35–0.4 mJy beam^{-1} per spectral channel.

ALMA visibilities have been calibrated using the CASA software (McMullin et al. 2007). The final continuum images and data cubes have been generated with the CASA task TCCLEAN using a natural weighting, which gives the optimum point-source sensitivity in the image plane. Final products have angular resolutions between 0.6 and 1.5 arcsec depending on the data sets (see Table 1). The *uv*-coverage of the observations results in a largest angular resolution between 1.7 and 5 arcsec depending on the observed frequencies. Continuum images have been obtained from the line-free channels of the four spectral windows that have been also used in the task UVCONTSUB to subtract the continuum emission in the *uv*-plane. The data cubes have been generated from the continuum-subtracted *uv* data sets.

In addition to the observations of our programme, we have searched in the ALMA archive for further public data sets. We have thus used the ALMA observations of the project 2015.1.01265.S (PI: R. Wang) targeting the CO(8–7) line at $\nu_{\rm rest} = 921.80$ GHz ($\nu_{\rm obs} = 131.63$ GHz) and the CO(9–8) line at $\nu_{\rm rest} = 1036.91$ GHz ($\nu_{\rm obs} = 148.06$ GHz) in J2310. The data sets will be presented by Shao et al. (2019) and in a forthcoming paper by Li et al. (in preparation). In this work, we present the continuum emissions at 132 and 141 GHz and the two CO lines with their relative luminosities. For J1319, we have benefited from continuum emission at 347 GHz observed in the ALMA project 2012.1.00391.S (PI: J. Gracia-Carpio). All retrieved observations have been reduced by following the ALMA pipeline released with the data sets and final image have been generated by adopting a natural weight scheme.

In addition to the ALMA data, we have collected from the literature all submillimetre/millimetre measurements associated with these two quasars and to J1148 (see Tables 1 and 2).

Table 2. Results of the SED fitting (assuming $k_0 = 0.45$ cm^2 g^{-1} and $\nu_0 = 250$ GHz) and CO observations.

	J2310	J1319	J1148
	Dust emission		
Log($M_{\rm dust}$/M$_\odot$)	8.75 ± 0.07	8.8 ± 0.2	8.5 ± 0.1
$T_{\rm dust}$ (K)	76 ± 3	66^{+15}_{-10}	75 ± 8
β	1.8 ± 0.1	1.5 ± 0.3	1.5 ± 0.2
$L_{\rm FIR}$ (10^{13} L$_\odot$)	2.5 ± 0.4	$1.6^{+1.3}_{-0.6}$	2.1 ± 0.7
	CO emission (10^8 L$_\odot$)		
CO(1–0)	–	–	$<0.72^{d}$
CO(2–1)	0.213 ± 0.002^{a}	–	0.125 ± 0.010^{e}
CO(3–2)	–	–	0.39 ± 0.04^{f}
CO(6–5)	5.5 ± 0.5^{b}	1.6 ± 0.3^{c}	2.5 ± 0.3^{d}
CO(7–6)	–	–	2.9 ± 0.3^{g}
CO(8–7)	7.1 ± 0.6	–	–
CO(9–8)	7.5 ± 0.9	–	–
CO(14–13)	–	$<1.8^{\ddagger}$	–
CO(17–16)	$<8.1^{\ddagger}$	$<2.6^{\ddagger}$	$4.9 \pm 1.1^{h\dagger}$
CO(19–18)	–	$<3.2^{\ddagger}$	–

Note. Reference: [a]Shao et al. (2019); [b]Feruglio et al. (2018); [c]Wang et al. (2013); [d]Bertoldi et al. (2003b); [e]Stefan et al. (2015); [f]Walter et al. (2003); [g]Riechers et al. (2009); and [h]Gallerani et al. (2014). [‡]Upper limits are estimated in an aperture of 1.4×1.4 arcsec^2, and spectral width of $\Delta v = 400$ km s^{-1} for J2310 and $\Delta v = 500$ km s^{-1} for J1319. [†]The CO(17–16) luminosity of J1148 accounts for the possible contamination by OH$^+$. See Gallerani et al. (2014) and Section 5.2 for further details.

4 RESULTS

4.1 Continuum emission

The continuum emission is detected with high level of significance ($>10\sigma$) in all ALMA data sets for both quasars (left-hand panels of Figs 1 and 2). The ALMA coordinates of the two sources are RA = 23:10:38.8994, Dec. = +18.55.19.83716 (J2310) and RA = 13:19:11.2879, Dec. = +09.50.51.526 (J1319) and are in agreement with those reported by previous works (Wang et al. 2013; Shao et al. 2017; Feruglio et al. 2018). The centre coordinates of the continuum emission of both sources are consistent with those estimated from the infrared *Y*-band images of *Hubble Space Telescope*, once the astrometry of the two observations has been aligned.

We analyse the continuum emission directly in the Fourier plane (hereafter *uv*-plane) by fitting the interferometric visibilities. We adopt a Sérsic radial profile (with fixed index $n = 1$) as a model for the continuum brightness and we assume axisymmetry to produce a 2D model image. We use the publicly available GALARIO package (Tazzari, Beaujean & Testi 2018) to compute the visibilities of the model image by sampling its Fourier transform in the same (u,v) points sampled by ALMA. The free parameters are the total flux density S_ν, the half-light radius $R_{\rm e}$, the position angle (PA, rotation on the plane of sky, defined east of north), the ellipticity (or disc inclination along the line of sight), and the (δRA, δDec.) offsets on sky with respect to the observations' phase centre. Since the (δRA, δDec.) are nuisance parameters, in the results we present here we marginalize over them. We perform the fit in a Bayesian framework, exploring the parameter space using the Markov chain Monte Carlo (MCMC) algorithm implemented in the EMCEE package (Foreman-Mackey et al. 2013). We assume uniform priors on the free parameters and a Gaussian likelihood $\mathcal{L} \propto \exp(-\chi^2/2)$, where $\chi^2 = \sum_{j=1}^{N} |V_{\rm mod,j} - V_{\rm obs,j}|^2 w_j$, with $V_{\rm mod,j}$ and $V_{\rm obs,j}$ being the model and the observed visibilities and w_j the weight associated to the jth visibility point. We use the GPU-accelerated GALARIO to compute $V_{\rm mod}$ from the model image determined by the free parameter values.

An example of the fit result for J2310(J1319) is given in Fig. 3 (Fig. A1), where we compare the model and the observed visibilities (real and imaginary part) as a function of the deprojected baseline (*uv*-distance). The drop in the real part of the visibilities with the *uv*-distance indicates that the continuum emission is spatially resolved in the current ALMA data set. The figure also shows that the observed continuum profile well matches the radial exponential model. We report the best-fitting results of both the data sets in Table 1. More details on the fit procedure using `galario` are given in Appendix A. We note that the results obtained with the visibility modelling are consistent with the flux densities and deconvolved size estimate measured both in the image plane by using the CASA task IMFIT and in the *uv*-plane by using the CASA task UVMODELFIT.

By combining all measurements from this work and literature, we infer an half-light radius of $R_{\rm e} = 0.113 \pm 0.008$ arcsec (0.66 ± 0.05 kpc) for J2310 and of $R_{\rm e} = 0.146 \pm 0.015$ arcsec (0.84 ± 0.09 kpc) for J1319. This indicates that at least 50 per cent of the dust mass is hosted in a compact region of radius <0.9 kpc.

4.2 FIR luminosities

We estimate the FIR luminosities and dust masses of the two quasars by combining our continuum data with previous ALMA, PdBI, Max-Planck-Millimeter-Bolometer (MAMBO), and Very Large Telescope (VLA) observations (Wang et al. 2011, 2013; Feruglio et al. 2018; Hashimoto et al. 2018), whose continuum flux densities are reported in Table 1.

The spectral energy distribution (SED) of dust emission can be represented with a modified blackbody function, which is also dubbed grey-body law, given by

$$S^{\rm obs}_{\nu_{\rm obs}} = S^{\rm obs}_{\nu/(1+z)} = \frac{\Omega}{(1+z)^3} B_\nu(T_{\rm dust})(1 - {\rm e}^{-\tau_\nu}), \quad (1)$$

where $S^{\rm obs}_{\nu_{\rm obs}}$ is the flux density measured at the observed frequency $\nu_{\rm obs} = \nu/(1+z)$, Ω is the solid angle subtended by the galaxy,[1] $B_\nu(T_{\rm dust})$ is the blackbody emission at the dust temperature $T_{\rm dust}$, and τ_ν is the dust optical depth. The optical depth can be expressed in the form

$$\tau_\nu = \Sigma_{\rm dust} k_\nu = \Sigma_{\rm dust} k_0 \left(\frac{\nu}{\nu_0}\right)^\beta, \quad (2)$$

where $\Sigma_{\rm dust}$ and k_ν are the surface mass density of dust and dust opacity (Draine & Lee 1984), respectively. The $\Sigma_{\rm dust}$ can be expressed in term of total dust mass ($M_{\rm dust}$) and the physical area of the galaxy ($A_{\rm galaxy}$): $\Sigma_{\rm dust} = M_{\rm dust}/A_{\rm galaxy}$ (da Cunha et al. 2013); the dust opacity k_ν depends on the emissivity index β, mass absorption coefficient k$_0$ and ν_0. The latter two terms, k$_0$ and ν_0, are usually assumed from either observations (e.g. Alton et al. 2004; Beelen et al. 2006) or dust models (e.g. Bianchi & Schneider 2007). In this work we assume k$_\nu$ $= 0.45(\nu/250\ {\rm GHz})^\beta$ cm^2 g^{-1} (Beelen et al. 2006).

In equation (1) we must also consider the contribution of the CMB emission since, at $z = 6$, the CMB temperature may be comparable

[1]The solid angle Ω can be also written as $\Omega = (1+z)^4 A_{\rm galaxy} D_L^{-2}$, where $A_{\rm galaxy}$ and D_L are the surface area and luminosity distance of the galaxy, respectively.

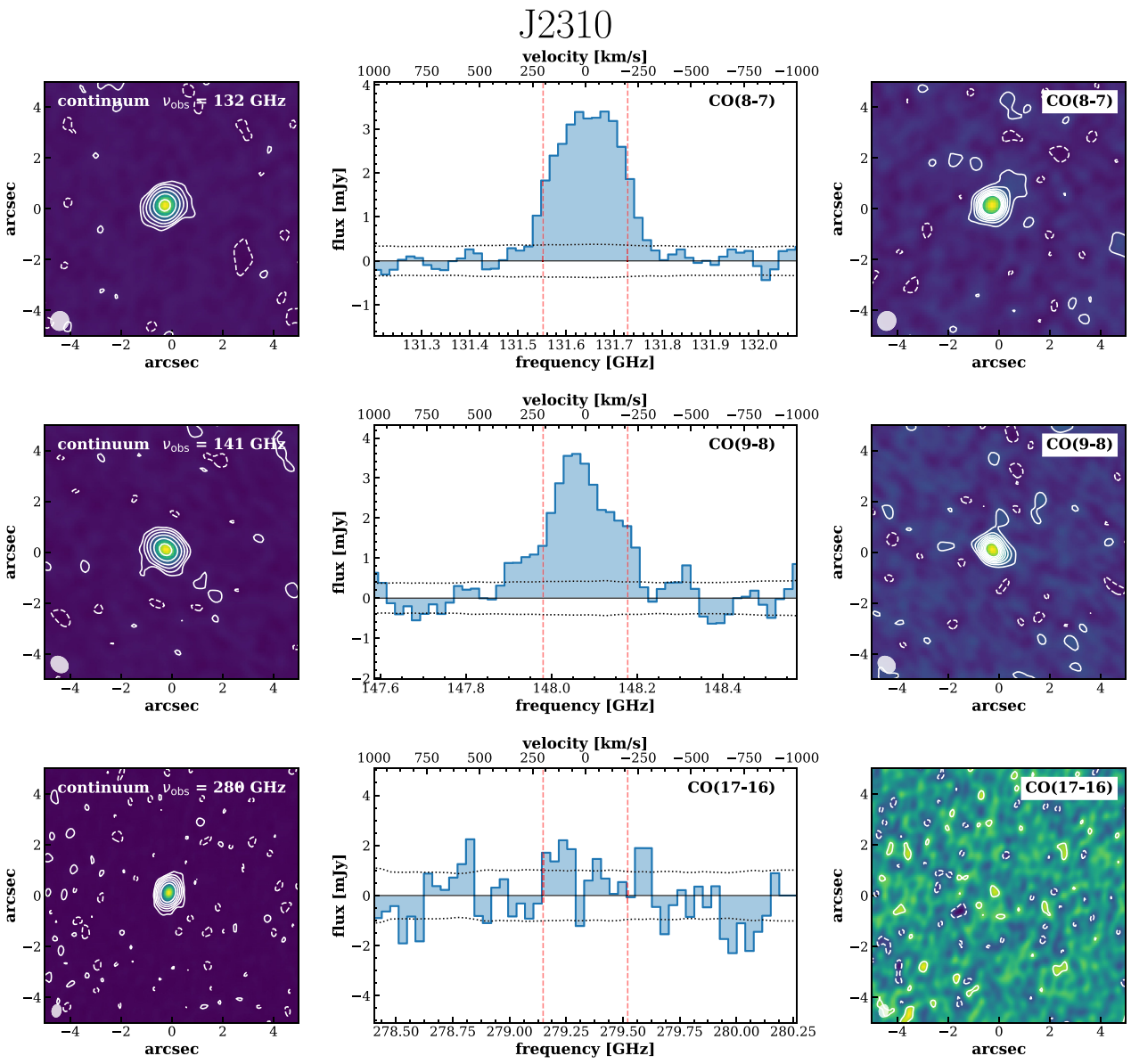

Figure 1. J2310. Left-hand panels: continuum emission maps at 132 GHz (top), 141 GHz (middle), and 280 GHz (bottom). Contours are plotted at levels of (−2, 2, 4, 8, 16, 32, 64) times σ. The rms noise level is 15, 15, and 42 μJy beam^{-1}, respectively, for the three maps. In each map, the ALMA beam is plotted on the bottom left-hand corner. Central panels: continuum subtracted spectra extracted from a region of radius 1.5 arcsec. From top to bottom we report the spectrum of CO(8–7), CO(9–8), and CO(17–16) . All spectra are rebinned at the same spectral resolution of 40 km s^{-1} and the horizontal dotted lines indicate the noise level as a function of frequency. Vertical dashed red lines represent the frequency/velocity range used to extract the flux map shown in the right-hand panels. Right-hand panels: flux maps of CO(8–7) (top), CO(9–8) (middle), and CO(17–16) (bottom). Emission is integrated in channels with $|v| < 200$ km s^{-1} relative to the frequency of the CO lines. Contours are shown in step of 2σ starting from $\pm 2\sigma$, where 1σ is 40, 40, and 70 mJy beam^{-1} km s^{-1}, respectively, for the three molecular lines.

(or even higher) to that of dust, thus affecting observations and measurements. An extensive discussion about the CMB effect on the dust emission has been already presented by da Cunha et al. (2013); in this section we only provide a quick review of their main results.

In addition to the galaxy radiation, CMB photons contribute to increase the dust temperature and boost the observed dust emission. The effect on the dust temperature is

$$T_{\rm dust}(z) = ((T_{\rm dust})^{4+\beta} + {T_0}^{4+\beta}[(1+z)^{4+\beta} - 1])^{\frac{1}{4+\beta}}, \quad (3)$$

where T_0 is the CMB temperature at $z = 0$, i.e. $T_0 = 2.73$ K (Fixsen et al. 1996). On the other hand, the CMB emission at high-z is a strong background against which the dust continuum emission is observed, thus reducing its detectability. The observed SED shape of dust emission can thus be expressed as

$$S^{\rm obs}_{\nu/(1+z)} = \frac{\Omega}{(1+z)^3}\,[B_\nu(T_{\rm dust}(z)) - B_\nu(T_{\rm CMB}(z))]\,(1 - {\rm e}^{-\tau_\nu}), \quad (4)$$

where $T_{\rm dust}(z)$ is given by equation (3) and $B_\nu(T_{\rm CMB}(z))$ is the blackbody emission of CMB at the temperature $T_{\rm CMB}(z) = T_0(1 + z)$.

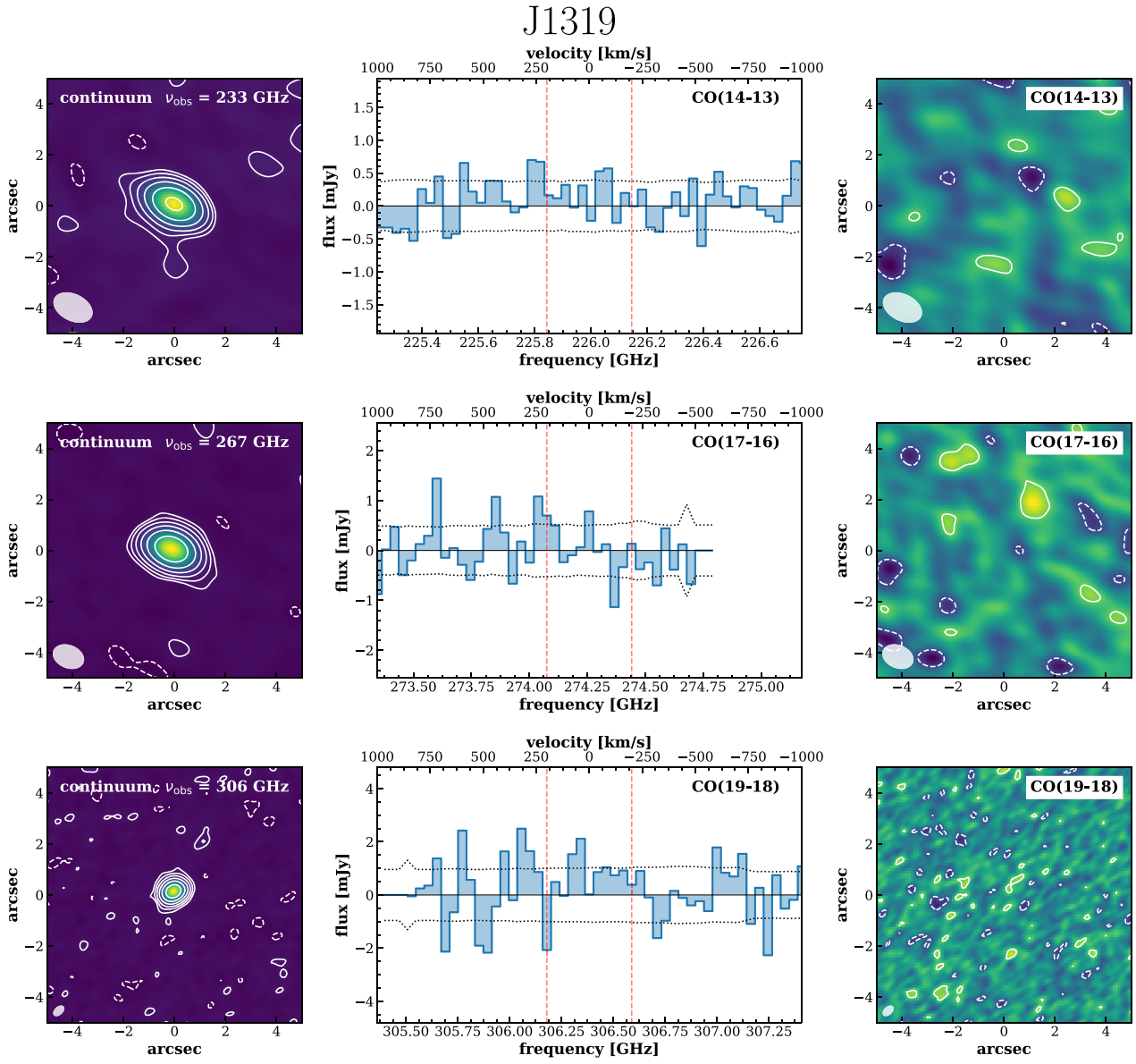

Figure 2. J1319. Left-hand panels: continuum emission maps at 233 GHz (top), 267 GHz (middle), and 306 GHz (bottom). Contours levels are [−4, −2, 2, 4, 8, 16, 32, 64, 128] times σ. The 1σ is 45, 43, and 42 μJy beam^{-1}, respectively, for the three maps. In each map, the ALMA beam is plotted on the bottom left-hand corner. Central panels: continuum subtracted spectra extracted from a region of radius 1.5 arcsec. From top to bottom we report the spectrum of CO(14–13), CO(17–16), and CO(19–18) . All spectra are rebinned at the same spectral resolution of 40 km s^{-1} and the horizontal dotted lines indicate the noise level as a function of frequency. Vertical dashed red lines represent the frequency/velocity range used to extract the flux map shown in the right-hand panels. Right-hand panels: flux maps of CO(14–13) (top), CO(17–16) (middle), and CO(19–18) (bottom). Emission is integrated in channels with $|v| < 200$ km s^{-1} relative to the frequency of the CO lines. Contours are shown in step of 2σ starting from $\pm 2\sigma$, where 1σ is 80, 80, and 60 mJy beam^{-1} km s^{-1}, respectively, for the three molecular lines.

We use equation (4) to fit the flux continuum densities measured in J2310 and J1319. We estimate the solid angle subtended by each galaxy from the continuum emission size inferred in Section 4.1 and then explore the three free parameters, M_{dust}, T_{dust}, and β, by using a MCMC algorithm to estimate the posterior probability distribution for the three-dimensional parameter space that defines our SED model. We employ uniform distributions for the priors, but we force $30 < T_{dust} < 90$ K and $1.0 < \beta < 2.0$ since these are the typical ranges observed in star-forming galaxies and quasars (Beelen et al. 2006).

Fig. 4 shows the results of the SED model fitting, Table 2 reports the best-fitting results, and Fig. 5 shows the confidence contours for the three free parameters obtained from a MCMC with 50 chains and 3000 trials. While the dust masses are well pinned down in both sources with errors smaller than 20 per cent, the emissivity index and dust temperature are constrained only in J2310, where the ALMA band 8 observations are present. We note that our best-fitting T_{dust} values for J2310 and J1319 are higher than the dust temperatures (T_{dust} = 40–50 K) inferred in previous works (Wang et al. 2013; Shao et al. 2019). This discrepancy can be explained by the different

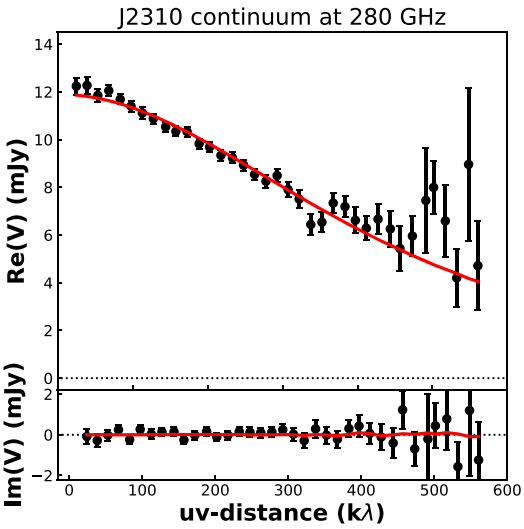

Figure 3. Comparison between the model and the observed visibilities (real and imaginary part) of the J2310 continuum emission at 280 GHz as a function of deprojected baseline (*uv*-distance). For the deprojection we used the inferred inclination and PA. The black dots are the observations, the red line shows the best-fitting model.

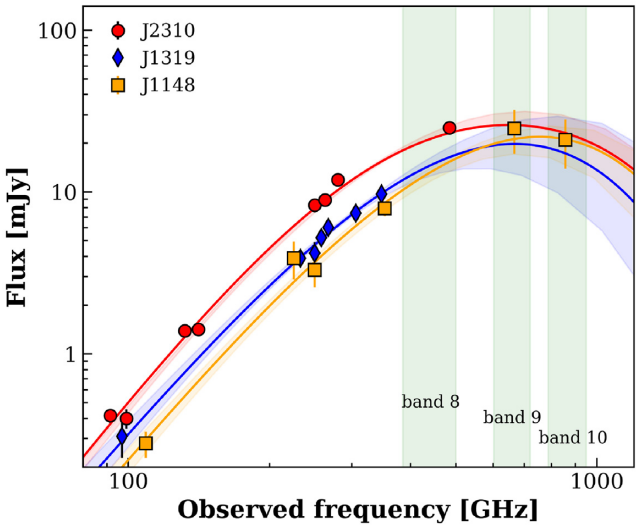

Figure 4. Spectral energy distribution of J2310 (red), J1319 (blue), and J1148 (orange). The observations are reported as circle, diamonds, and square marks, while the lines indicate the SED best-fitting models. The vertical shaded green region shows the range of frequency covered by ALMA band 8, 9, and 10, which are fundamental to constrain dust properties in high-z sources (see text).

assumptions adopted on the dust opacity when modelling the SED. Indeed, previous works have assumed an optically thin ($\tau_\nu << 1$) modified blackbody profile to fit the continuum observations. Here, we are instead also considering dust emission attenuation. In fact, the dust masses and continuum sizes of our AGN host galaxies provide $\tau_\nu > 0.5$ at $\nu_{\rm obs} > 300$ GHz, thus making the optically thin approximation not valid at higher frequencies. For comparison, in Appendix B we report the best-fitting results in the optical

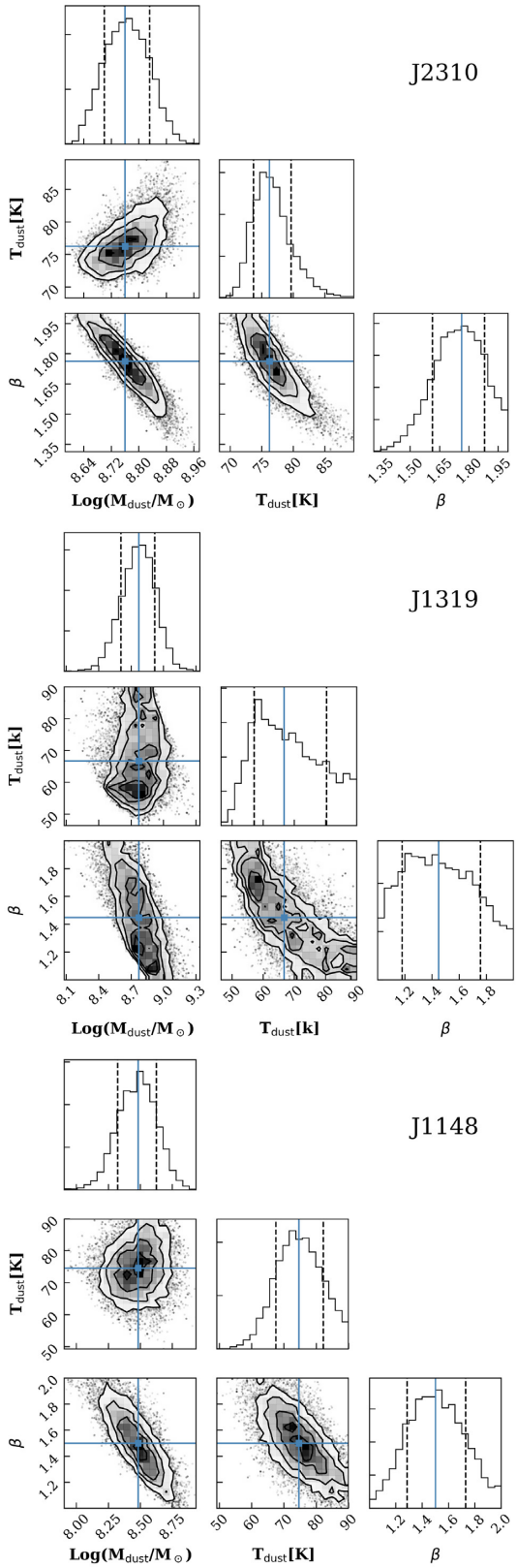

Figure 5. Corner plots showing the three-dimensional posterior probability distributions of $M_{\rm dust}$, $T_{\rm dust}$, and β for J2310 (top panel), J1319 (middle panel), and J1148 (bottom panel). Blue lines indicate the best-fitting parameter, while the dashed lines show the 16 and 84 per cent percentiles for each parameter. The lack of high-frequency observations does not allow us to constrain the $T_{\rm dust}$ and β of J1319.

Table 3. Quasar properties.

	J2310	J1319	J1148
M_{1450} [a]	−27.61	−27.12	-27.80
Log(SFR$_{FIR}$/M$_\odot$ yr^{-1})[b]	3.61 ± 0.06	3.4 ± 0.3	3.5 ± 0.2
$L_{[C\,II]}$ [c] [10^9 L$_\odot$]	8.7 ± 1.4	4.4 ± 0.9	37 ± 9
L_{X-ray} [d] [10^{45} erg s^{-1}]	$0.7^{+0.5}_{-0.3}$	–	$1.4^{+0.4}_{-0.3}$
M_{BH} [e] [10^9 M$_\odot$]	1.8	2.7	3

[a]Absolute magnitude at 1450 Å from Fan et al. (2003), Mortlock et al. (2009), and Jiang et al. (2016). [b]SFR from FIR luminosity. [c][C II] luminosities from Wang et al. (2013) and Cicone et al. (2015). [d]X-ray luminosity between 2 and 10 keV from Gallerani et al. (2017b) and Vito et al. (2019). [e]Black hole (BH) mass by Willott, McLure & Jarvis (2003), Shao et al. (2017), and Feruglio et al. (2018).

thin assumptions, which are in agreement with those reported by previous studies (Wang et al. 2013; Shao et al. 2019).

The shadowed red and blue regions in Fig. 4 give an indication of the β and T_{dust} degeneration associated with the best-fitting models. While the shaded regions shrink at lower frequencies (<400 GHz), the uncertainties enlarge close to the peak of the curve. This indicates that high-frequency observations, as that in band 8 for J2319, are fundamental to constrain the properties of the dust in the distant Universe. Observations in ALMA band 8, 9, and 10, which are the highest frequency bands in the baseline ALMA project, are thus crucial to compute the dust temperature in the first billion years of the Universe.

We perform the SED fitting of J1148 as well by using the same assumptions made for the other two quasars and taking into account the CMB contribution. We retrieve from the literature all flux continuum densities (Bertoldi et al. 2003a; Walter et al. 2003; Riechers et al. 2009; Cicone et al. 2015) at the wavelength $\lambda_{rest} > 50$ μm where the emission is powered mainly by star formation activity in the host galaxy and the contribution from the AGN is negligible (Leipski et al. 2013). Given the presence of a serendipity source at 10.5 arcsec, we give less weight to those continuum measurements of J1148 that may be contaminated by the emission of a serendipity source (Cicone et al. 2015). The results of the Bayesian fit is reported in Figs 4 and 5 and Table 2.

We estimate the FIR luminosities by integrating the best-fitting models from 8 to 1000 μm rest frame for the three quasars. Despite the comparable FIR luminosities ($L_{FIR} \sim 10^{13}$ L$_\odot$), from the SED fitting it results that the dust temperature of J1148 is 2σ higher than that inferred for J2310, possibly due to a stronger radiation field in the former. For all quasars we turn the FIR luminosities into SFR by using the relations from Kennicutt & Evans (2012). All quasars have SFR > 1000 M$_\odot$ yr^{-1} (see Table 3).

4.3 High-J CO emission

4.3.1 CO measurements in J2310

While the continuum emission is detected in all ALMA data sets of J2310, the detection of $J_{up} > 7$ CO lines is limited only to the two lower transitions, CO(8–7) and CO(9–8) (Fig. 1; see also Li et al., in preparation). Both CO lines have a line width of 380 km s^{-1} and a beam-deconvolved size of 0.50 ± 0.12 arcsec (∼3 kpc at $z = 6$). We measure integrated flux densities of 1.49 ± 0.13 Jy km s^{-1} for CO(8–7) and 1.41 ± 0.16 Jy km s^{-1} for CO(9–8) that correspond to a luminosity of (7.1 ± 0.6) × 10^8 L$_\odot$ and (7.5 ± 0.9) × 10^8 L$_\odot$, respectively (Table 2).

The flux map of the CO(17–16) emission, which has been obtained by integrating the data cube within ±200 km s^{-1} from the expected frequency of the $J_{up} = 17$ CO line, shows a marginal detection of 2σ at the location of the quasar. To be conservative we estimate a 3σ upper limit on its flux density in an aperture of 1.4 × 1.4 arcsec^2,[2] yielding $L_{CO(17-16)} < 8.1 \times 10^8$ L$_\odot$.

4.3.2 CO measurements in J1319

At the location of the quasar J1319 all three ALMA observations do not reveal any signature of $J_{up} > 7$ CO emission. The right-hand panels of Fig. 2 show the flux maps obtained by collapsing the data cubes over a channel width of 500 km s^{-1} that is comparable to the line widths observed in the CO(6–5) and [C II] lines (Wang et al. 2013; Shao et al. 2017). In Table 2, we report the 3σ upper limit, measured in an aperture size as large as 1.4 × 1.4 arcsec^2, on each CO transition analysed in this work.

5 CO SLED

In this section, we compute the CO SLED resulting from the ALMA data presented in this work and from the other CO measurements in literature. We then compare our findings with the CO SLEDs observed in low-z starburst galaxies and AGN, and the CO SLEDs measured in other $z \sim 6$ quasars.

5.1 CO(6–5)-normalized CO SLED

In the left-hand panel of Fig. 6, we show the CO SLED (normalized to the CO(6–5) line) of J2310, J1319, J1148 (Bertoldi et al. 2003b; Riechers et al. 2009; Gallerani et al. 2014; Stefan et al. 2015), and the three $z \sim 6$ quasars by Venemans et al. (2017b). The blue and red shaded regions represent the averaged CO(6–5)-normalized CO SLEDs from low-z starburst galaxies and AGN, respectively (Table C1; Mashian et al. 2015; Rosenberg et al. 2015; Mingozzi et al. 2018). Despite the large uncertainties, the CO SLED of the AGN population is characterized by a slightly different shape with respect to the one of starburst galaxies. At high-J ($J_{up} \geq 13$) the starburst CO SLED is less excited and the CO emission steadily declines at $J_{up} > 8$, while the AGN CO SLED seems to reach the peak at $8 \leq J_{up} \leq 10$ and declines afterwards.

The CO luminosities and upper limits measured for J2310 and J1319 are consistent with both AGN and starburst CO SLEDs. Although the $L_{CO(8-7)}/L_{CO(6-5)}$ and $L_{CO(9-8)}/L_{CO(6-5)}$ ratios measured in J2310 are slightly higher relative to the typical ratios observed in starburst galaxies, they are still consistent (within 1σ) with the CO SLED shape of both populations (AGN and starburst galaxies). The same is true for the three $z \sim 6$ quasars by Venemans et al. (2017b) that have $1 \lesssim L_{CO(7-6)}/L_{CO(6-5)} \lesssim 4$, consistently with low-$z$ observations.

For what concerns J1148, at lower J_{up} (<7), the CO(6–5)-normalized SLED is also similar to that observed in local AGN and starburst populations. However this quasar is characterized by an exceptionally strong CO(17–16) emission line that is >3σ larger than the averaged CO SLED of both populations. The CO ratio is

[2]Current ALMA observations of J2310 and J1319 have different angular resolutions. To compare the CO upper limits, the flux densities have been estimated from the same size aperture as large as the ALMA beam of the poorest angular resolution data set (∼1.4 arcsec).

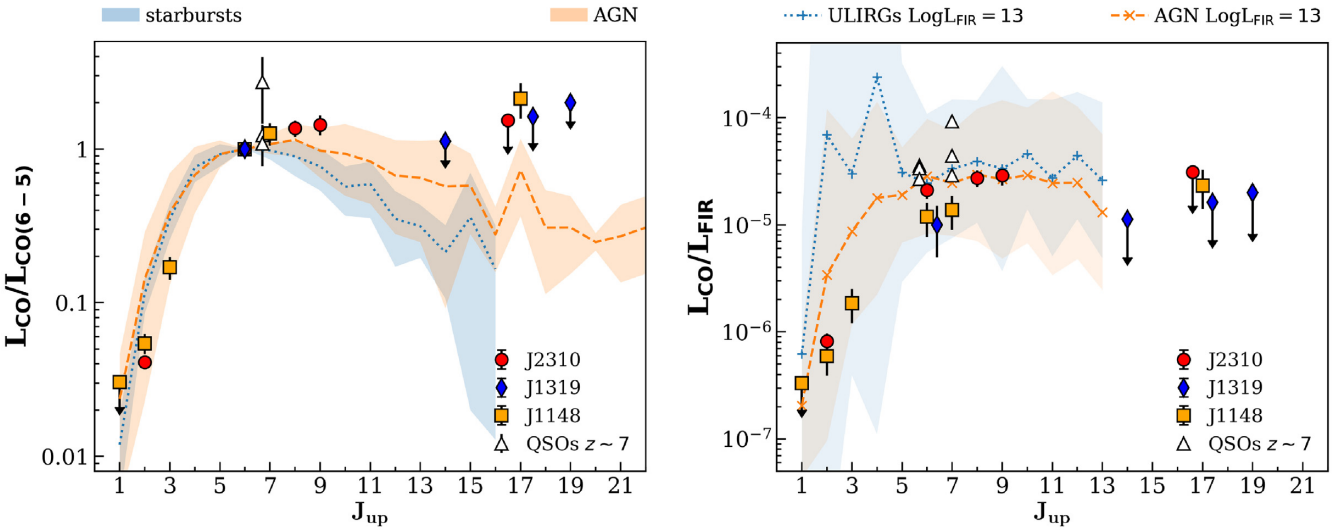

Figure 6. Left-hand panel: average CO SLED of local AGN (dashed red line) and starburst galaxies (dotted blue line) from literature (Mashian et al. 2015; Rosenberg et al. 2015; Mingozzi et al. 2018). The list of the local galaxies is reported in Table C1. CO SLEDs are normalized to the CO(6–5) line. The shaded regions show the variance in each observed line. Orange, red, and blue marks indicate the CO measurements of J1148, J2310, and J1319, respectively. Right-hand panel: CO SLED normalized by FIR luminosity of individual quasar: J1148 (orange), J2310 (red), and J1319 (blue). The dashed and dotted lines indicate the average L_{CO}/L_{FIR} ratio estimated from the each J_{up} relations $\log(L'_{CO}) = \alpha \log(L_{FIR}) + \beta$ inferred for AGN and ULIRGs, respectively (Kamenetzky et al. 2016).

also $\sim 1\sigma$ higher than the upper limits on the CO(17–16)/CO(6–5) ratios estimated for J2310 and J1319.

We further discuss the origin of the discrepancy between J1148 and other $z \sim 6$ quasars in Section 6. Here, we mention that the CO(17–16) emission detected in J1148 may be contaminated by the presence of several flanking OH^+ lines falling within few hundreds km s^{-1} of the CO line. These lines have been observed in local nearby AGN host galaxies (Hailey-Dunsheath et al. 2012; González-Alfonso et al. 2013) and seem to be more luminous in presence of fast outflowing gas and XDRs (González-Alfonso et al. 2013, 2018). By fitting with a double Gaussian profile the emission detected in J1148, Gallerani et al. (2014) estimate that ∼40 per cent of the measured luminosity can be contaminated by OH^+ line emission. We thus perform, both in J2310 and J1319, a blind line search (see Carniani et al. 2017a,b, for details) to look for possible OH^+ + CO emissions at the location and redshift of the two quasars, but we do not find any emission with an intensity $>2\sigma$.

To interpret the results found in J2310 we have repeated the analysis done in Gallerani et al. (2014) by adopting the PDR/XDR models by Meijerink & Spaans (2005) and Meijerink et al. (2007). The same analysis is hampered in J1319 given that, in this source, only the CO(6–5) line has been detected. We found that a PDR model alone can fairly explain the intensity of the CO lines observed in J2310. In particular, our analysis suggests that the molecular gas of this source is characterized by a density $n \sim 4 \times 10^5$ cm^{-3}, irradiated by a FUV flux $G_0 \sim 3 \times 10^3$ (in Habing units of 1.6×10^{-3} erg s^{-1} cm^{-2}). No information on XDR can be inferred from our J2310 observations: this is expected, since the effect of X-ray photons on the molecular gas excitation can be disentangled from the one due to FUV photons only if CO lines with $J_{up} > 10$ are available (e.g. Schleicher et al. 2010).

5.2 L_{FIR}-normalized CO SLED

Tight L_{CO}–L_{FIR} correlations have been found over several orders of magnitude from low- to high-J CO lines ($4 < J_{up} < 13$; Greve et al. 2014; Liu et al. 2015; Kamenetzky et al. 2016; Lu et al. 2017) suggesting the average CO gas excitation conditions are mainly associated with star formation activity, while AGN seem to have negligible impact on the CO SLED shape, at least for $J_{up} \leq 10$–13. We therefore investigate the CO excitation conditions in our quasars by normalizing their CO SLED to the FIR luminosity and by comparing the results with $z < 1$ star-forming galaxies and AGN hosts (Kamenetzky et al. 2016). The right-hand panel of Fig. 6 shows the FIR-normalized CO SLED for J2310, J1319, J1148, the three $z \sim 6$ quasars by Venemans et al. (2017b), and for local starbursts and AGN host galaxies.

We find that the L_{CO}/L_{FIR} ratios of the three quasars are consistent, within the uncertainties, with the FIR-normalized SLEDs observed locally, suggesting that the CO emission with $J_{up} < 7$ is powered by the star formation activity in the host galaxies. A similar conclusion has been stated by Venemans et al. (2017b) for their three quasars at $z \sim 6$. By combining CO, [C II], and [C I] observations, Venemans et al. (2017b) conclude that CO emission in their three quasars predominantly arises in PDRs heated by young stars, and exclude substantial contribution from XDRs.

From the right-hand panel of Fig. 6, we also note that the CO/L_{FIR} ratios, up to $J_{up} = 7$, of both J1319 and J1148 are below the line ratios observed in J2310 and in the other high-z quasars despite their comparable FIR luminosities. Such a discrepancy could indicate the heterogeneous properties of PDRs among these high-z quasars. Indeed the intensity of the CO line depends on the metallicity, gas temperature, molecular density, and radiation field strength (e.g. Uzgil et al. 2016; Vallini et al. 2018). In addition low CO-to-FIR line ratios can be also explained by an overestimation of the FIR luminosity. Both AGN emission in the rest-frame mid-IR wavelengths (8 and 40 μm) and the presence of polycyclic aromatic hydrocarbon (PAH) features could affect the FIR luminosity estimates (e.g. Greve et al. 2014). In J1148 the AGN contamination at $\lambda_{rest} > 50$ μm ($\nu_{obs} \lessapprox 850$ GHz) is highly uncertain and may vary between 20 and 70 per cent (Leipski et al. 2013; Schneider et al. 2015). The AGN contamination may explain the magnitude of the CO/L_{FIR} discrepancy. A deficiency in the molecular gas content could also explain the low CO-to-FIR line

with respect to J2310. As also observed in other lower z quasars characterized by extended ionized outflows (Carniani et al. 2015, 2017b; Brusa et al. 2018), where a substantial gas fraction has been is removed from the host galaxy by AGN winds. In the case of J1148 this scenario is supported by the detection of broad wings in the [C II] line profile, suggesting the presence of fast outflowing gas in the host galaxy (Maiolino et al. 2012; Cicone et al. 2015). In particular, Cicone et al. (2015) found that J1148 hosts a powerful outflows with a mass outflow rate >1000 $M_\odot$ yr^{-1} large enough to clear out all the gas content of the galaxy in less than $\sim$6 Myr. We further note that, for this quasar, Stefan et al. (2015) infer a molecular gas mass from the CO(2–1) emission of $M_{H_2} = 2.6 \times 10^{10}$ $M_\odot$ that is smaller than that measured in J2310 ($M_{H_2} = 4.2 \times 10^{10}$ $M_\odot$; Shao et al. 2019). Given the high dust mass of J1319 (Table 2), we exclude that the outflow scenario would explain the low CO-to-FIR line ratios in this quasar.

6 DISCUSSION

The nature of the discrepancy between the high CO(17–16) line luminosity observed in J1148 and local sources/high-z quasars is unclear, both because of the complexity of the physical processes involved in the molecular gas excitation and the paucity of observational data. From the theoretical point of view, the emergence of bright high-J ($J_{up} > 13$) CO lines can be associated both with extreme star formation, and AGN activity, and shocks induced by merging/outflows/supernova-driven winds. In Table 3, we report the properties of J2310, J1319, and J1148 that are more relevant in this context.

(i) *Star formation.* The properties of J1148, J2310, and J1310 are quite similar in terms of FIR emission (Fig. 4). Assuming that dust heating is dominated by stars, the resulting SFRs among the three quasars are comparable (Table 2). If high-J CO lines are predominantly excited by star formation activity, we should have observed in J2310 and J1319 CO(17–16) lines as luminous as in J1148.

(ii) *AGN activity.* Strong high-J CO lines can be excited in XDRs (Meijerink et al. 2007; Spaans & Meijerink 2008; Schleicher et al. 2010; van der Werf et al. 2010). Given the similarity among BH masses ($M_{BH} \sim 2$–3×10^9 $M_\odot$) and AGN luminosities ($-27.80 < M_{1450} < -27.12$) of the three quasars, we do not expect their X-ray luminosities to differ much. Still, J1148 is the only quasar among the three for which X-ray observations are available (Gallerani et al. 2017b). Thus, we cannot exclude that the high luminosity of the CO(17–16) detected in J1148 can be associated with its X-ray radiation (Gallerani et al. 2014). This interpretation is favoured by the fact that the X-ray luminosity ($L_{X\text{-ray}} = 1.4 \times 10^{45}$ erg s^{-1}) of J1148 is higher than that of J2310 ($L_{X\text{-ray}} = 7 \times 10^{44}$ erg s^{-1}; Vito et al. 2019) suggesting the presence of a stronger X-ray radiation in J1148.

(iii) *Shocks.* High temperatures associated with shock-dominated regions can also be responsible for boosting the luminosity of high-J CO lines (Panuzzo et al. 2010; Hailey-Dunsheath et al. 2012; Meijerink et al. 2013). In this context, it is remarkable that, while J1148 exhibits a massive, powerful outflow with a mass outflow rate >1000 $M_\odot$ yr^{-1} (Maiolino et al. 2012; Cicone et al. 2015), in the other sources no such strong outflows have been found (Carniani et al. in preparation). High-resolution numerical simulations show that AGN feedback can trigger outflows as powerful as the one revealed in J1148 (Barai et al. 2018) and shock heat large quantity of gas to the high temperatures required for the excitation of high-J CO lines (Costa et al. 2014, 2018 Costa, Sijacki & Haehnelt 2015; Barai et al. 2018). Nevertheless, these simulations lack both the chemistry of molecular hydrogen (e.g. Pallottini et al. 2017a,b) and radiative transfer of X-ray photons (e.g. Kakiichi et al. 2017), thus hampering a realistic comparison with observations.

To summarize, our analysis disfavours a scenario in which the high CO(17–16) luminosity observed in J1148 is driven by PDRs, even accounting for the possible contamination by OH^+ emission. In the case of CO SLEDs excited by star formation, even in the case of high SFRs, the CO(6–5)- and FIR-normalized CO SLEDs are expected to decreases at high-J with a peak at $6 < J_{up} < 8$, as observed in the low-z starburst sample and in J2310. Other mechanism associated with AGN (XDRs, AGN-driven outflows) is more likely responsible for the excitation of high-J transitions.

However, the lack of CO(17–16) detections in J2310 and J1319 suggests that AGN activity is not always associated with strong high-J CO lines.

7 CONCLUSIONS

We have presented ALMA observations of dust continuum and molecular CO line emission in two quasars at $z \sim 6$, J1319 and J2310. We have also retrieved the CO and dust measurements for J1148 in order to compare the properties of these three quasars and understand the origin of their CO emission. Our main findings are as follows.

(i) By fitting the continuum emission directly in the *uv*-plane, we have found that the bulk of dust emission arises from a compact (<0.9 kpc) region of the host galaxies. We have estimated a half-light radius of $R_e = (0.66 \pm 0.05)$ kpc for J2310 and $R_e = (0.84 \pm 0.09)$ kpc for J1319.

(ii) We have performed a SED fitting on our two quasars and on J1148 using millimetre observations from literature and from this work and taking into account the impact of CMB on dust emission at high redshift. The dust properties, such as FIR luminosity, dust mass, temperature, and emissivity index, of the J2310 and J1148 have been estimated with an uncertainties lower than 20 per cent (Table 2). The lack of high-frequency ($\nu > 400$ GHz) observations for J1319 have led to large uncertainties on dust temperature, which spans over a range $50 \lesssim T_{dust} \lesssim 80$ K. With a SFR > 1000 $M_\odot$ yr^{-1} and $L_{FIR} > 10^{13}$ $L_\odot$, the host galaxies of the analysed quasars are in a starburst phase of their evolution.

(iii) In addition to the dust continuum emission we have discussed the observations of CO(9–8), CO(8–7), and CO(17–16) for J2310, in which we have found a clear detection only for the first two lines. For what concerns J1319, we have presented ALMA observations of the CO(14–13), CO(17–16), and CO(19–18) lines and reported no detection in all the CO transitions observed.

(iv) We have computed the CO SLEDs normalized to the CO(6–5) line and FIR luminosity for J2310, J1319, and J1148 and compared our results both with local starburst galaxies and AGN, and with other $z \sim 6$ quasars. For $J_{up} < 9$, the CO(6–5)- and FIR-normalized CO SLEDs of $z \sim 6$ quasars are consistent with low-z sources. However we note that the CO/FIR ratios of J1319 and J1148 are $\sim$2 times lower than those measured in J2310. This discrepancy could indicate heterogeneous ISM properties among high-z quasars. We have also suggested that the difference of L_{CO}/L_{FIR} between J2310 and J1148 can be explained by either a FIR AGN contamination or a lower molecular gas content in J1148. Latter scenario is supported by the presence of fast outflowing gas

that can remove molecular gas from the host galaxies of these quasars.

(v) The upper limits on the CO(17–16) transitions for J2310 and J1319 are consistent with those observed in local AGN and starburst galaxies; vice versa the 3σ upper limits on the CO(17–16)/CO(6–5) ratio measured in these sources are 1σ lower than that measured in J1148. Mechanisms associated with AGN (XDRs, AGN-driven outflows) are likely responsible for the excitation of this high-J CO transition and for the higher CO(17–16) luminosity measured in J1148.

In summary the no detection of high-J ($J_{up} \geq 14$) CO transitions in the quasars J2310 and J1319 reveals that AGN activity is not always associated with luminous ($> 10^8$ $L_\odot$) highly excited CO emission lines. The detection of $J_{up} > 8$ lines in $z \sim 6$ quasars, complemented by X-ray observations and supported by dedicated high-resolution numerical simulations (including AGN-driven feedback, molecular hydrogen chemistry, and radiative transfer of X-ray photons), represents the best strategy to progress in the field and provide the optimal chances to understand the processes responsible for molecular gas excitation.

ACKNOWLEDGEMENTS

This paper makes use of the following ALMA data: ADS/JAO.ALMA#2013.1.00462.S, ADS/JAO.ALMA#2015.1.01265.S, and ADS/JAO.ALMA#2012.1.00391.S. ALMA is a partnership of ESO (representing its member states), NSF (USA), and NINS (Japan), together with NRC (Canada), MOST and ASIAA (Taiwan), and KASI (Republic of Korea), in cooperation with the Republic of Chile. The Joint ALMA Observatory is operated by ESO, AUI/NRAO, and NAOJ. AF and SC acknowledge support from the ERC Advanced Grant INTERSTELLAR H2020/740120. This work reflects only the authors' view and the European Research Commission is not responsible for information it contains. LV acknowledges funding from the European Union's Horizon 2020 research and innovation program under the Marie Skłodowska-Curie Grant agreement no. 746119. MT has been supported by the DISCSIM project, grant agreement 341137 funded by the European Research Council under ERC-2013-ADG. RM acknowledges support from the ERC Advanced Grant 695671 'QUENCH' and from the Science and Technology Facilities Council (STFC). CC and CF acknowledge support from the European Union Horizon 2020 research and innovation programme under the Marie Skłodowska-Curie grant agreement no. 664931.

We are grateful to the anonymous referee for her/his comments. We finally acknowledge the contribution of Paolo Comaschi to this work.

REFERENCES

Alton P. B., Xilouris E. M., Misiriotis A., Dasyra K. M., Dumke M., 2004, A&A, 425, 109
Aravena M. et al., 2016, MNRAS, 457, 4406
Bañados E. et al., 2016, ApJS, 227, 11
Bañados E. et al., 2018, Nature, 553, 473
Barai P., Gallerani S., Pallottini A., Ferrara A., Marconi A., Cicone C., Maiolino R., Carniani S., 2018, MNRAS, 473, 4003
Beelen A., Cox P., Benford D. J., Dowell C. D., Kovács A., Bertoldi F., Omont A., Carilli C. L., 2006, ApJ, 642, 694
Bertoldi F., Carilli C. L., Cox P., Fan X., Strauss M. A., Beelen A., Omont A., Zylka R., 2003a, A&A, 406, L55
Bertoldi F. et al., 2003b, A&A, 409, L47
Bianchi S., Schneider R., 2007, MNRAS, 378, 973
Bischetti M., Maiolino R., Fiore S. C. F., Piconcelli E., Fluetsch A., 2018, A&A, in press (arXiv:1806.00786)
Brusa M. et al., 2018, A&A, 612, A29
Carilli C. L., Walter F., 2013, ARA&A, 51, 105
Carniani S. et al., 2013, A&A, 559, A29
Carniani S. et al., 2015, A&A, 580, A102
Carniani S. et al., 2017a, A&A, 605, A42
Carniani S. et al., 2017b, A&A, 605, A105
Cicone C. et al., 2015, A&A, 574, A14
Costa T., Sijacki D., Trenti M., Haehnelt M. G., 2014, MNRAS, 439, 2146
Costa T., Sijacki D., Haehnelt M. G., 2015, MNRAS, 448, L30
Costa T., Rosdahl J., Sijacki D., Haehnelt M. G., 2018, MNRAS, 479, 2079
da Cunha E. et al., 2013, ApJ, 766, 13
Decarli R. et al., 2017, Nature, 545, 457
Decarli R. et al., 2018, ApJ, 854, 97
De Rosa G., Decarli R., Walter F., Fan X., Jiang L., Kurk J., Pasquali A., Rix H. W., 2011, ApJ, 739, 56
Di Matteo T., Khandai N., DeGraf C., Feng Y., Croft R. A. C., Lopez J., Springel V., 2012, ApJ, 745, L29
Draine B. T., Lee H. M., 1984, ApJ, 285, 89
Egami E. et al., 2018, Publ. Astron. Soc. Aust., 35, e048
Fan X. et al., 2003, AJ, 125, 1649
Feruglio C. et al., 2018, A&A, 619, A39
Fixsen D. J., Cheng E. S., Gales J. M., Mather J. C., Shafer R. A., Wright E. L., 1996, ApJ, 473, 576
Foreman-Mackey D., Hogg D. W., Lang D., Goodman J., 2013, PASP, 125, 306
Gallerani S. et al., 2012, A&A, 543, A114
Gallerani S., Ferrara A., Neri R., Maiolino R., 2014, MNRAS, 445, 2848
Gallerani S., Fan X., Maiolino R., Pacucci F., 2017a, Publ. Astron. Soc. Aust., 34, e022
Gallerani S. et al., 2017b, MNRAS, 467, 3590
Genzel R. et al., 2015, ApJ, 800, 20
Giallongo E. et al., 2015, A&A, 578, A83
González-Alfonso E. et al., 2013, A&A, 550, A25
González-Alfonso E. et al., 2018, ApJ, 857, 66
Greve T. R. et al., 2014, ApJ, 794, 142
Hailey-Dunsheath S. et al., 2012, ApJ, 755, 57
Hashimoto T., Inoue A. K., Tamura Y., Matsuo H., Mawatari K., Yamaguchi Y., 2018, PASJ, in press (arXiv:1811.00030)
Jiang L., Fan X., Vestergaard M., Kurk J. D., Walter F., Kelly B. C., Strauss M. A., 2007, AJ, 134, 1150
Jiang L., McGreer I. D., Fan X., Strauss M. A., Bañados E., Becker R. H., Bian F., Farnsworth K., 2016, ApJ, 833, 222
Kakiichi K., Graziani L., Ciardi B., Meiksin A., Compostella M., Eide M. B., Zaroubi S., 2017, MNRAS, 468, 3718
Kakkad D. et al., 2017, MNRAS, 468, 4205
Kamenetzky J., Rangwala N., Glenn J., Maloney P. R., Conley A., 2016, ApJ, 829, 93
Kennicutt R. C., Evans N. J., 2012, ARA&A, 50, 531
Kormendy J., Ho L. C., 2013, ARA&A, 51, 511
Kulkarni G., Worseck G., Hennawi J. F., 2019, MNRAS, 488, 1035
Kurk J. D., Walter F., Fan X., Jiang L., Riechers D. A., Rix H.-W., Pentericci L., Strauss, 2007, ApJ, 669, 32
Lamastra A., Menci N., Maiolino R., Fiore F., Merloni A., 2010, MNRAS, 405, 29
Leipski C. et al., 2013, ApJ, 772, 103
Li Y. et al., 2007, ApJ, 665, 187
Liu D., Gao Y., Isaak K., Daddi E., Yang C., Lu N., van der Werf P., 2015, ApJ, 810, L14

Lu N. et al., 2017, ApJS, 230, 1
McMullin J. P., Waters B., Schiebel D., Young W., Golap K., 2007, in Shaw R. A., Hill F., Bell D. J., eds, ASP Conf. Ser. Vol. 376, Astronomical Data Analysis Software and Systems XVI. Astron. Soc. Pac., San Francisco, p. 127
Madau P., Haardt F., 2015, ApJ, 813, L8
Maiolino R. et al., 2012, MNRAS, 425, L66
Manti S., Gallerani S., Ferrara A., Greig B., Feruglio C., 2017, MNRAS, 466, 1160
Mashian N., Sturm E., Sternberg A., Janssen A., Hailey-Dunsheath S., Fischer J., Contursi A., González-Alfonso E., 2015, ApJ, 802, 81
Matsuoka Y. et al., 2016, ApJ, 828, 26
Matsuoka Y. et al., 2018, PASJ, 70, S35
Mazzucchelli C. et al., 2017, ApJ, 849, 91
Meijerink R., Spaans M., 2005, A&A, 436, 397
Meijerink R., Spaans M., Israel F. P., 2007, A&A, 461, 793
Meijerink R. et al., 2013, ApJ, 762, L16
Mingozzi M. et al., 2018, MNRAS, 474, 3640
Mitra S., Choudhury T. R., Ferrara A., 2018, MNRAS, 473, 1416
Mortlock D. J., Patel M., Warren S. J., Venemans B. P., McMahon R. G., Hewett P. C., Simpson C., Sharp R. G., 2009, A&A, 505, 97
Narayanan D. et al., 2008, ApJS, 174, 13
Obreschkow D., Heywood I., Klöckner H.-R., Rawlings S., 2009, ApJ, 702, 1321
Pallottini A., Ferrara A., Gallerani S., Vallini L., Maiolino R., Salvadori S., 2017a, MNRAS, 465, 2540
Pallottini A., Ferrara A., Bovino S., Vallini L., Gallerani S., Maiolino R., Salvadori S., 2017b, MNRAS, 471, 4128
Panuzzo P. et al., 2010, A&A, 518, L37
Parsa S., Dunlop J. S., McLure R. J., 2018, MNRAS, 474, 2904
Pilbratt G. L. et al., 2010, A&A, 518, L1
Planck CollaborationXIII, 2016, A&A, 594, A13
Poglitsch A. et al., 2010, A&A, 518, L2
Qin Y. et al., 2017, MNRAS, 472, 2009
Richings A. J., Faucher-Giguère C.-A., 2018, MNRAS, 474, 3673
Riechers D. A. et al., 2009, ApJ, 703, 1338
Riechers D. A. et al., 2013, Nature, 496, 329
Rosenberg M. J. F. et al., 2015, ApJ, 801, 72
Schleicher D. R. G., Spaans M., Klessen R. S., 2010, A&A, 513, A7
Schneider R., Bianchi S., Valiante R., Risaliti G., Salvadori S., 2015, A&A, 579, A60
Shao Y. et al., 2017, ApJ, 845, 138
Shao Y. et al., 2019, ApJ, 876, 99
Spaans M., Meijerink R., 2008, ApJ, 678, L5
Spinoglio L. et al., 2017, Publ. Astron. Soc. Aust., 34, e057
Stefan I. I. et al., 2015, MNRAS, 451, 1713
Tazzari M., Beaujean F., Testi L., 2018, MNRAS, 476, 4527
Tunnard R., Greve T. R., 2016, ApJ, 819, 161
Uzgil B. D., Bradford C. M., Hailey-Dunsheath S., Maloney P. R., Aguirre J. E., 2016, ApJ, 832, 209
Valiante R., Schneider R., Salvadori S., Gallerani S., 2014, MNRAS, 444, 2442
Valiante R., Agarwal B., Habouzit M., Pezzulli E., 2017, Publ. Astron. Soc. Aust., 34, e031
Vallini L., Pallottini A., Ferrara A., Gallerani S., Sobacchi E., Behrens C., 2018, MNRAS, 473, 271
van der Werf P. P. et al., 2010, A&A, 518, L42
Venemans B. P. et al., 2017a, ApJ, 837, 146
Venemans B. P. et al., 2017b, ApJ, 845, 154
Vito F. et al., 2019, preprint (arXiv:1908.09849)
Volonteri M., 2010, A&AR, 18, 279
Volonteri M., Gnedin N. Y., 2009, ApJ, 703, 2113
Volonteri M., Stark D. P., 2011, MNRAS, 417, 2085
Walter F. et al., 2003, Nature, 424, 406
Wang R. et al., 2010, ApJ, 714, 699
Wang R., Wagg J., Carilli C. L., Neri R., Walter F., Omont A., Riechers D. A., Bertoldi F., 2011, AJ, 142, 101
Wang R., Wagg J., Carilli C. L., Walter F., Lentati L., Fan X., Riechers D. A., Bertoldi F., 2013, ApJ, 773, 44
Weiß A., Downes D., Neri R., Walter F., Henkel C., Wilner D. J., Wagg J., Wiklind T., 2007, A&A, 467, 955
Willott C. J., McLure R. J., Jarvis M. J., 2003, ApJ, 587, L15
Willott C. J. et al., 2010, AJ, 140, 546
Wu X.-B. et al., 2015, Nature, 518, 512

APPENDIX A: VISIBILITY ANALYSIS

In Section 4.1, we presented the analysis of the continuum emission. Here we report more details of the fit procedure.

To perform the fits we follow the quick start example reported in the documentation of GALARIO.[3]

(i) We extract the channel-averaged continuum visibilities from the ALMA measurement set using the function EXPORT_UVTABLE included in the publicly available UVPLOT package.[4]

(ii) We define our brightness model as the Sersic profile:

$$I(R) = I_{\rm e} \exp\left\{-b_n\left[\left(\frac{R}{R_{\rm e}}\right)^{(1/n)} - 1\right]\right\}, \quad \text{(A1)}$$

where $R_{\rm e}$ is the effective (half-light) radius, $I_{\rm e}$ is the surface brightness at $R = R_{\rm e}$, and b_n is such that $\Gamma(2n) = 2\gamma(2n, b_n)$ and we fix the index $n = 1$ (i.e. exponential profile). We compute the brightness profile $I(R)$ on a radial grid ranging from 0.0001 to 10 arcsec, with spacing 0.001 arcsec.

(iii) We define the parameter ranges explored by the 40 walkers in the MCMC ensemble sampler. We use log-uniform priors for $I_{\rm e}$ and $R_{\rm e}$, $p(\log I_{\rm e}) = U(-5, 1)$, $p(\log R_{\rm e}) = U(-2, 0)$, and uniform priors for the other free parameters, $p(i) = U(0°, 90°)$, $p(\mathrm{PA}) = U(180°, 360°)$.

After the MCMC chain has converged, we assess the goodness of the fit by comparing the best-fitting model and the observations, directly in the plane of the measurements. An immediate way of checking whether a model fits the interferometric data is to produce a so-called *uv*-plot, namely the azimuthal average of the visibilities as a function of deprojected baseline (*uv*-distance). Fig. 3 in Section 4.1 and Fig. A1 here show the *uv*-plot comparing the best-fitting models and the observed visibilities of J2310 and J1319.

Although the complex visibilities are defined on the *uv*-plane $V(u, v)$, it is often convenient to represent them in bins of deprojected *uv*-distance $\rho = \sqrt{u^2 + v^2}$. It is worth noting that the fit performed with GALARIO allowed us to fit *each single* observed (u_j, v_j) visibility point by computing the corresponding $V_{\rm mod}(u_j, v_j)$ of a given model image; the azimuthally averaged view of the best-fitting model and of the data given in the *uv*-plot serves as a benchmark of the goodness of the fit and is inevitably showing less data than it was actually used for the fit.

To produce the *uv*-plot we used the UVPLOT package following the instructions in the GALARIO quick start example (see link in the footnotes). To deproject the visibilities we assume inclination and position angle inferred from the fit.

[3] https://mtazzari.github.io/galario/quickstart.html
[4] https://github.com/mtazzari/uvplot

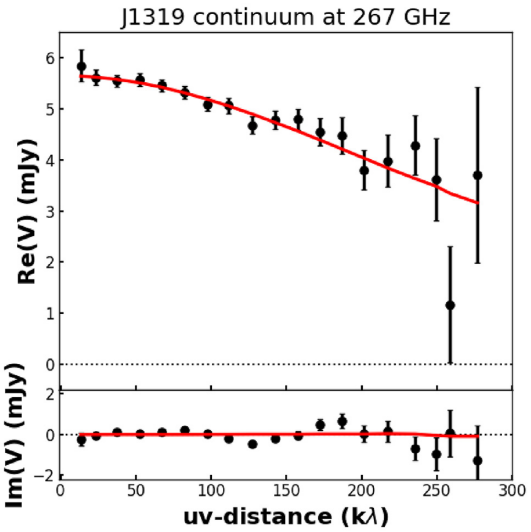

Figure A1. Comparison between the model and the observed visibilities (real and imaginary part) of the J1319 continuum emission at 267 GHz as a function of deprojected baseline (*uv*-distance). For the deprojection we used the inferred inclination and PA. The black dots are the observations, the red line shows the best-fitting model.

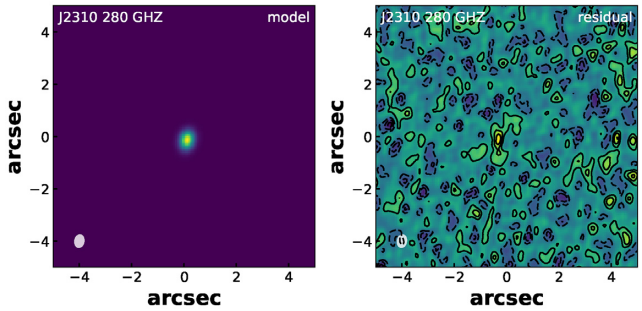

Figure A2. Synthesized image of the model (left) and residual (right) visibilities. Contours in the right-hand panel are in steps of $1(-1)\sigma$ starting from $\sigma = 42$ μJy beam^{-1}, which is the rms noise.

Another way to assess the goodness of the fit is to produce synthesized images of the residual visibilities, namely to compute $V_{\rm res}(u_j, v_j) = V_{\rm obs}(u_j, v_j) - V_{\rm mod}(u_j, v_j)$ for the best-fitting model and then obtaining the CLEANed image corresponding to $V_{\rm res}$. Figs A2 and A3 show the synthesized images of the model and of the residual visibilities. In both cases, the extremely low levels of the residuals (within the 3σ noise levels) indicate that the models closely match the measurements.

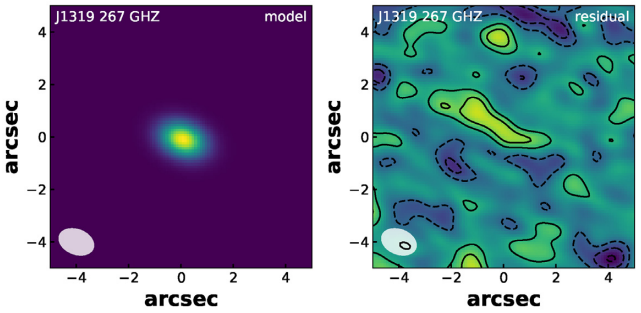

Figure A3. Synthesized image of the residual visibilities. Contours in the right-hand panel are in steps of $1(-1)\sigma$ starting from $\sigma = 43$ μJy beam^{-1}, which is the rms noise.

APPENDIX B: OPTICALLY THIN ASSUMPTION FOR DUST SED MODEL

In the optically thin assumption ($\tau_\nu << 1$) equation (4) can be rewritten as

$$S^{\rm obs}_{\nu/(1+z)} \simeq \frac{\Omega}{(1+z)^3}\left[B_\nu(T_{\rm dust}(z)) - B_\nu(T_{\rm CMB}(z)\right]\tau_\nu$$
$$= \frac{(1+z)A_{\rm galaxy}}{D_L^2}\left[B_\nu(T_{\rm dust}(z)) - B_\nu(T_{\rm CMB}(z)\right]\frac{M_{\rm dust}}{A_{\rm galaxy}}k_\nu$$
$$= \frac{(1+z)M_{\rm dust}}{D_L^2}\left[B_\nu(T_{\rm dust}(z)) - B_\nu(T_{\rm CMB}(z)\right]k_\nu. \quad \text{(B1)}$$

Similarly to the analysis performed in Section 4.2 we assume $k_\nu = 0.45(\nu/250\ {\rm GHz})^\beta$ cm^2 g^{-1} and fit the continuum measurements of the three AGN host galaxies. The best-fitting results (Table B1), which have been obtained from a MCMC analysis, are in agreement with those from previous studies (Leipski et al. 2013; Wang et al. 2013; Shao et al. 2019).

By comparing the results obtained from equation (4), in which dust opacity is accounted for, and those from the optical thin model (equation B1), we note that while the dust mass and emissivity index measurements are consistent within 3σ, the best-fitting dust temperature values strongly depend on the dust opacity assumptions.

Table B1. Results of the SED fitting (assuming $k_0 = 0.45\,{\rm cm^2\,g^{-1}}$, $\nu_0 = 250$ GHz, and optical thin modified blackbody profile (equation B1).

	J2310	J1319	J1148
Dust parameters (optical thin assumption)			
$\log(M_{\rm dust}/{\rm M}_\odot)$	9.08 ± 0.06	8.9 ± 0.2	8.6 ± 0.1
$T_{\rm dust}$ (K)	41^{+5}_{-3}	55 ± 15	63^{+12}_{-10}
β	1.7 ± 0.1	$1.3^{+0.3}_{-0.2}$	1.4 ± 0.3
$L_{\rm FIR}$ (10^{13} L$_\odot$)	$1.6^{+0.4}_{-0.3}$	$1.7^{+1.6}_{-0.7}$	$2.3^{+0.8}_{-0.6}$

APPENDIX C: LOCAL CO SLEDS

Table C1 shows the list of local AGN and starbursts galaxies that have been adopted to obtain the average local CO SLEDs. The intensity of CO lines of each galaxy is reported by Rosenberg et al. (2015), Mashian et al. (2015), and Mingozzi et al. (2018).

Table C1. List of local AGN and starburst galaxies having CO multiline observations.

AGN	Starburst galaxies
NGC 4945	NGC 253
Circinus	M83
Mrk 231	M82
NGC 6240	IC 694
NGC 3690	NGC 4418
NGC 1068	MCG+12-02-001
NGC 34	NGC 1614
IC 1623	NGC 2146
NGC 1365	NGC 3256
IRASF 05189−2524	ESO 320−G030
NGC 2623	ESO 173−G015
Arp 229	IRASF 17207−0014
IRAS 13120−5453	IC 4687
NGC 5135	NGC 7552
Mrk 273	NGC 7771
NGC 6240	Mrk 331
NGC 7469	

Note. References: Rosenberg et al. (2015), Mashian et al. (2015), and Mingozzi et al. (2018).

This paper has been typeset from a TEX/LATEX file prepared by the author.